nature chemistry

Article

https://doi.org/10.1038/s41557-026-02104-x

Isolated and H_2-reduced Anderson clusters catalyse low-temperature hydrogenation of CO_2 to methanol

Received: 2 April 2025

Accepted: 17 February 2026

Published online: 23 March 2026

Check for updates

Qin Liu[1,5], S. M. Gulam Rabbani[2,5], Zhenhao Hou[3,5], Zhihengyu Chen[4] ✉, Haofan Yang[1], Wentuan Bi[1,3] ✉, Karena W. Chapman[4], Rachel B. Getman[2] ✉ & Joseph T. Hupp[1] ✉

CO_2 hydrogenation, especially to methanol, is crucial to establishing sustainable closed-loop systems for carbon utilization. However, the difficulties of CO_2 activation at low temperatures and the ambiguity of structure–activity correlations are obstacles to reducing the energy consumption of the hydrogenation process. Here we report that molecularly defined Anderson $PtMo_6O_{24}$ clusters, sited within a robust metal–organic framework, are catalytic for low-temperature CO_2 hydrogenation. The performance of the cluster showed no signs of decay in either its activity or methanol selectivity over 3,600 h at 180 °C. It also achieves a per-pass yield exceeding that of state-of-the-art heterogeneous catalysts under similar conditions. Combined in situ spectroscopy and density functional theory calculations demonstrated that CH_3OH formation is dominated by the reverse water–gas shift and subsequent CO* hydrogenation pathway, while the HCOO* pathway may serve as a supplementary route. The well-defined cluster structure offers an ideal model for elucidating structure–activity correlations and opens exciting avenues for the rational design of high-activity, low-temperature catalysts for CO_2 hydrogenation.

The conversion of CO_2, a major greenhouse gas, into valuable chemicals is a promising solution for establishing sustainable closed-loop systems and thereby addressing the challenge of climate change. Methanol is among the most valuable products of CO_2 conversion because it is an important and versatile feedstock for chemical manufacturing and energy source[1,2]. CO_2 hydrogenation to methanol is an exothermic process ($CO_2 + 3H_2 \rightarrow CH_3OH + H_2O$, $\Delta H_{298K} = -49.4$ kJ mol^{-1}) and higher temperatures are thermodynamically less favourable for methanol synthesis. Consequently, the development of catalysts that enable low-temperature operation has been vigorously pursued.

Benchmark $Cu/ZnO/Al_2O_3$ catalysts generally operate at high temperatures (≥250 °C), which can lead to high energy consumption and low CH_3OH selectivity[3]. Introducing H_2-activation components (for example, Pd and Ni) onto metal oxides catalysts such as In_2O_3/ZrO_2 and ZnO/ZrO_2 can improve catalytic activity at relatively lower temperatures (200–250 °C). However, it often comes at the cost of reduced methanol selectivity due to excessive hydrogenation of CO_2 to methane or its reduction to CO through the reverse water–gas shift (RWGS) reaction[4,5]. The complexity of such heterogeneous catalysts, which contain a variety of active sites on metal particles, metal oxides, supports and at their interfaces, has made it

[1]Department of Chemistry, Northwestern University, Evanston, IL, USA. [2]Department of Chemical and Biomolecular Engineering, The Ohio State University, Columbus, OH, USA. [3]Institute of Energy, Hefei Comprehensive National Science Center (Anhui Energy Laboratory), Hefei, China. [4]Department of Chemistry, Stony Brook University, Stony Brook, NY, USA. [5]These authors contributed equally: Qin Liu, S. M. Gulam Rabbani, Zhenhao Hou. ✉e-mail: zchen96@stanford.edu; bwintuan@gmail.com; getman.11@osu.edu; j-hupp@northwestern.edu

challenging to establish clear correlations between catalyst structure and performance[6,7].

Results and discussion

Catalytic performance

Geometric or electronic confinement of metal heteroatoms within molecularly precise polyoxometalate clusters, combined with confinement of these clusters within a porous crystalline framework, transforms heterogeneous gas–solid catalysis into quasi-homogeneous catalysis, creating ideal, uniform model systems for studying active sites via in situ spectroscopies[8,9]. Here, we report that $PtMo_6O_{24}$@NU1K (Supplementary Tables 1 and 2 and Supplementary Figs. 1–6), in which $PtMo_6O_{24}$ clusters were encapsulated in the *c*-pore of the Zr-based metal–organic framework (MOF) NU1000 (abbreviated as NU1K) via a facile impregnation process[10,11] (Fig. 1a), functions as an efficient and stable catalyst for low-temperature CO_2 hydrogenation to methanol. The catalytic performance of the $PtMo_6O_{24}$@NU1K catalyst showed high CH_3OH activity compared with previously reported Pt-based catalysts, which resulted in the realization of continuous methanol synthesis at low temperature.

CO_2 hydrogenation to methanol over a H_2-reduced $PtMo_6O_{24}$@NU1K ($PtMo_6O_{24}$@NU1K-R) can be initiated even at room temperature, as supported by in situ diffuse reflectance infrared Fourier transform spectroscopy (DRIFTS), which indicated the appearance of CO* and CH_3O* peaks as the mixture of CO_2 and H_2 passed through the catalyst at room temperature[12,13] (Supplementary Fig. 7). By contrast, under an identical gaseous hourly space velocity (GHSV) over the commercial $Cu/ZnO/Al_2O_3$ catalyst, as the benchmark for this reaction, methanol did not begin to form until the temperature reaches 140 °C (Fig. 1b). Under identical reaction conditions, as the temperature was varied, $PtMo_6O_{24}$@NU1K always delivered a higher net space–time yield for methanol than did $Cu/ZnO/Al_2O_3$ (Fig. 1b). The $PtMo_6O_{24}$@NU1K catalyst showed a conversion range of 1.6–20.4% and a selectivity range of 81–64% for CO_2 hydrogenation to methanol in the temperature range of 100–200 °C. It achieved a methanol per-pass yield range of 1.2–13.1% from 100 °C to 200 °C, which surpasses other state-of-the-art catalysts reported in the literature under similar reaction conditions under 200 °C (≤200 °C)[12–22] (Fig. 1c and Supplementary Table 3). Tests of the long-term stability of the MOF-enshrouded catalyst (that is, 3,600 h at 180 °C) showed no signs of decay in either activity (16.6% average conversion) or selectivity (79.0% average CH_3OH selectivity) (Fig. 1d). Scanning transmission electron microscopy (STEM) images show that the size and morphology of $PtMo_6O_{24}$@NU1K crystallites are well maintained post-reaction (Supplementary Figs. 8 and 9). No aggregated nanoparticles or clusters were observed on the exterior surfaces. This indicates that $PtMo_6O_{24}$@NU1K is robust for the low-temperature hydrogenation of CO_2 to methanol. The current selectivity, while not yet ideal, is partially compensated by exceptional stability that extends catalyst lifespan and reduces replacement downtime. This advantage supports its potential in specific process scenarios requiring ultralong operation cycles, with improving selectivity remaining a core goal for future research.

By contrast, $PtMo_6O_{24}/ZrO_2$ and Pt@NU1K were deliberately selected as control samples with similar Pt loading amounts for systematic comparison. Since NU1K is a Zr-based MOF, ZrO_2 was chosen as a conventional oxide support to evaluate whether the MOF confinement effect (rather than mere Zr-related interactions) is critical. The as-synthesized $PtMo_6O_{24}/ZrO_2$ exhibited a low CO_2 conversion of 3.9% with a low CH_3OH selectivity of 3.3% at 180 °C (Fig. 1d and Supplementary Fig. 10). The TEM image revealed that without MOF nanoconfinement, $PtMo_6O_{24}$ clusters aggregated into large nanoparticles of around 10 nm on ZrO_2 support after catalysis (Supplementary Fig. 11), exposing fewer active sites and leading to substantially lower activity. This highlights the indispensable role of NU1K's porous structure in stabilizing dispersed clusters. Pt@NU1K, which consists of 2-nm Pt nanoparticles uniformly dispersed on NU1K (Supplementary Fig. 12), showed negligible activity, with only 0.6% CO_2 conversion and 9.3% CH_3OH selectivity at 180 °C (Fig. 1d). The absence of MoO_x in Pt@NU1K allowed us to decouple the contribution of synergistic Pt–Mo interactions. The inferior performance of Pt@NU1K underscores the importance of MoO_x in modulating Pt's electronic state and catalytic behaviour. Under identical reaction conditions, these Pt-based reference samples exhibited much lower activity with CO as the dominant product. By contrast, $PtMo_6O_{24}$@NU1K demonstrated two orders of magnitude higher yield with methanol being the primary product (Supplementary Fig. 10).

To demonstrate the uniqueness of the synergistic effect between Pt and Mo in selectively producing methanol, two other Pt-based polyoxometalates (POMs), PtV_9O_{28} and PtW_6O_{24}, were successfully confined within the *c*-pores of NU1K, as comparative catalysts for CO_2 hydrogenation[23,24] (Supplementary Figs. 13–22). At 180 °C, the CO_2 conversion rates of PtV_9O_{28}@NU1K and PtW_6O_{24}@NU1K were 2.2% and 2.3%, with methanol selectivities of 31.3% and 41.0%, respectively (Fig. 1d). Both the activity and methanol selectivity of these catalysts were considerably lower than those of $PtMo_6O_{24}$@NU1K under the same reaction conditions, highlighting the unique advantage of the $PtMo_6O_{24}$ cluster in selectively generating methanol. In addition, Anderson-type polyoxometalate clusters incorporating other transition or main-group metals, namely $ZnMo_6O_{24}$ and $AlMo_6O_{24}$, were also synthesized and encapsulated into the *c*-pores of NU1K for comparative CO_2 hydrogenation tests[25,26] (Supplementary Figs. 13 and 23–27). The results showed that these clusters exhibited almost no catalytic activity at low temperatures, with CO_2 conversion remaining below 1.0% even at 200 °C (Supplementary Table 3). The observed negligible CO_2 hydrogenation activity (conversion <1.0% at 200 °C) is probably attributable to the inherently weak hydrogen dissociation capability of these base metals. These results collectively substantiate Pt's irreplaceability in facilitating the catalytic cycle, while the MOF matrix enhances stability and site accessibility.

To elucidate the role of MOF-NU1K in the catalytic reaction, we compared $PtMo_6O_{24}$@NU1K to unsupported $PtMo_6O_{24}$, and to the cluster supported by three structurally similar MOFs: NU901, NU1008 and Hf-NU1K (Supplementary Fig. 28). At 180 °C, the CO_2 conversion of pristine $PtMo_6O_{24}$ without NU1K confinement is only 3.6%, much lower than the 15.7% achieved by the NU1K-confined single-cluster $PtMo_6O_{24}$ (Fig. 1d). This is mainly attributed to the very low specific surface area and lack of porosity of pristine $PtMo_6O_{24}$ (less than 10 $m^2 g^{-1}$), which prevent reactant gas molecules from accessing the vast majority of clusters, thereby limiting catalytic performance (Fig. 1a). NU901 is a polymorph of NU1K, sharing the same metal-oxide nodes and organic linkers, but differing in topology. NU901 contains 12 Å diamond-shaped micropores, whereas NU1K features 31 Å hexagonal mesopores and 12 Å triangular micropores[27] (Supplementary Figs. 29–32). The *c*-pores of NU901, however, are identical to those of NU1K and thus present identical sites for immobilizing catalytic clusters. The CO_2 conversion and methanol selectivity of $PtMo_6O_{24}$@NU901 were 9.0% and 55.0%, respectively, both lower than those of $PtMo_6O_{24}$@NU1K (Fig. 1d). This performance difference may be attributed to the less favourable mass transfer of reactant and product molecules within micropores compared with mesopores. NU1008 shares the same topology as NU1K but differs in the organic linkers: NU1K uses tetratopic 1,3,6,8-(*p*-benzoate)pyrene ($TBAPy^{4-}$) linkers, while NU1008 employs 1,2,4,5-tetrakis(4-carboxylated-phenyl)-3,6-dibromobenzene ($TCPB^{4-}$) linkers. This compositional variation results in smaller *c*-pore dimensions (4 Å × 10 Å) in NU1008 compared with those in NU1K (8 Å × 10 Å) (ref. 28) (Supplementary Figs. 33–36) and permits the POM to be sited only in a more constrained way. Although NU1008 possesses mesopores that facilitate molecular diffusion, the CO_2 conversion and methanol selectivity of $PtMo_6O_{24}$@NU1008 were 12.1% and 61.5%, respectively, slightly lower than those of $PtMo_6O_{24}$@NU1K (Fig. 1d). These results suggest that the narrower *c*-pores may restrict effective contact between

https://doi.org/10.1038/s41557-026-02104-x

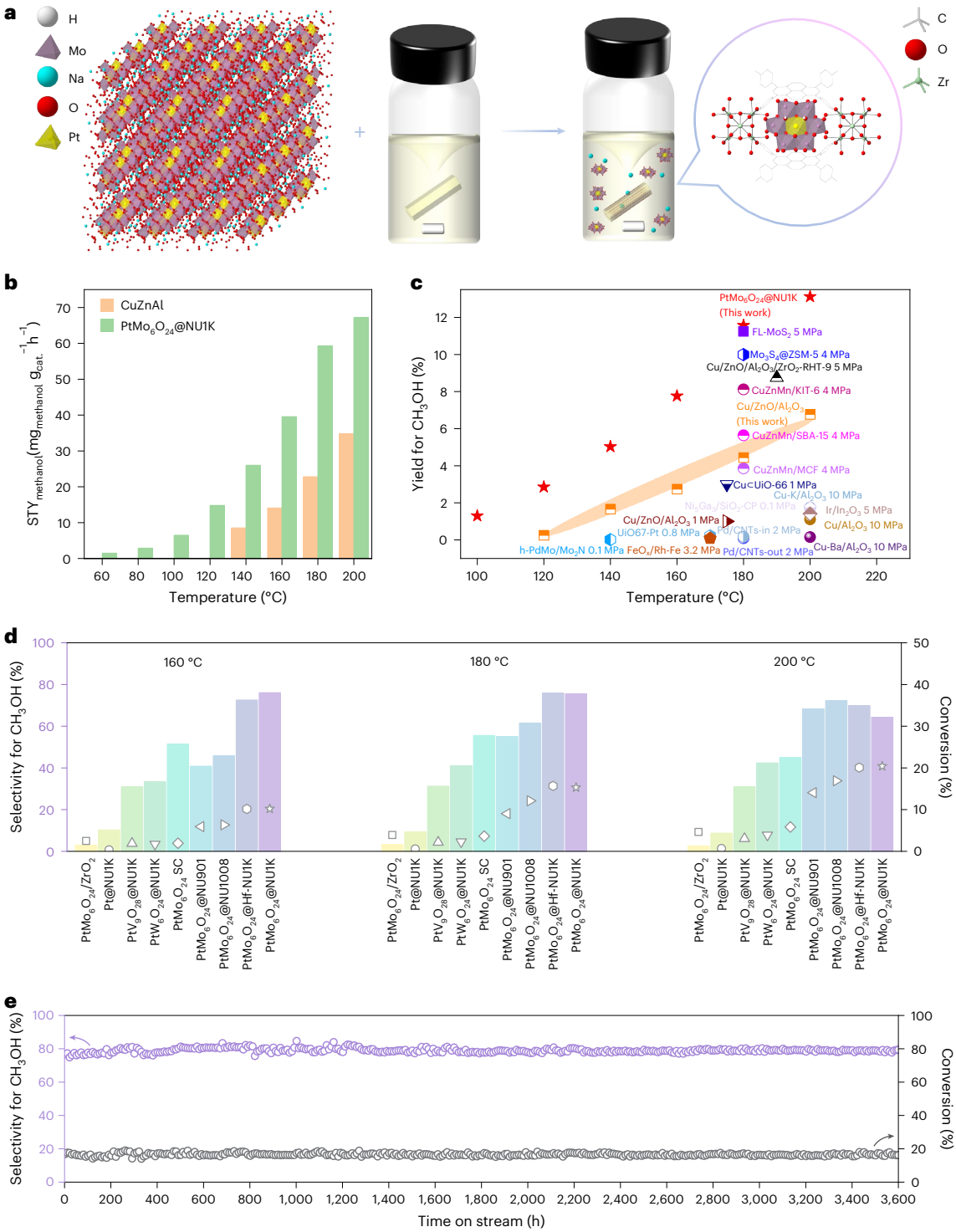

Fig. 1 | Catalytic properties of different catalysts in CO_2 hydrogenation to methanol. a, A flow chart for the preparation of $PtMo_6O_{24}$@NU1K. **b**, A comparison of the net $STY_{methanol}$ (calculated based on the amount of catalyst) on the $Cu/ZnO/Al_2O_3$ (CuZnAl) and $PtMo_6O_{24}$@NU1K catalysts from 100 °C to 200 °C at a GHSV of 1,500 ml $g_{cat.}^{-1}$ h^{-1}. **c**, A comparison of the per-pass yields over $PtMo_6O_{24}$@NU1K and other state-of-the-art catalysts under 200 °C (see Supplementary Table 3 for details). **d**, CO_2 conversion and product selectivity over Pt@NU1K, $PtMo_6O_{24}/ZrO_2$, PtV_9O_{28}@NU1K, PtW_6O_{24}@NU1K, $PtMo_6O_{24}$ SC, $PtMo_6O_{24}$@NU901, $PtMo_6O_{24}$@NU1008, $PtMo_6O_{24}$@Hf-NU1K and $PtMo_6O_{24}$@NU1K catalysts at 160 °C, 180 °C and 200 °C, respectively. **e**, Stability testing of $PtMo_6O_{24}$@NU1K in CO_2 hydrogenation at 1,500 ml $g_{cat.}^{-1}$ h^{-1}, with selectivity and conversion monitored over 3,600 h. The activity tests were conducted using a tubular fixed-bed reactor at 50 bar with an H_2/CO_2 ratio of 3:1.

gas molecules and the reactive centre of the $PtMo_6O_{24}$ cluster. Hf-NU1K has the same topology, and essentially the same pore dimensions, as NU1K but differs in the chemical composition of the metal-oxide nodes, which are $Hf_6(\mu_3\text{-}O)_4(\mu_3\text{-}OH)_4(H_2O)_4(OH)_4^{8+}$ and $Zr_6(\mu_3\text{-}O)_4(\mu_3\text{-}OH)_4(H_2O)_4(OH)_4^{8+}$, respectively[29] (Supplementary Figs. 37–40). The CO_2 conversion and methanol selectivity of $PtMo_6O_{24}$@Hf-NU1K were 15.7% and 75.9%, respectively, comparable to those of $PtMo_6O_{24}$@NU1K (Fig. 1d). These results indicate that the primary active sites for the catalytic reaction are probably the $PtMo_6O_{24}$ clusters located within the *c*-pores, rather than the zirconium-oxide nodes.

https://doi.org/10.1038/s41557-026-02104-x

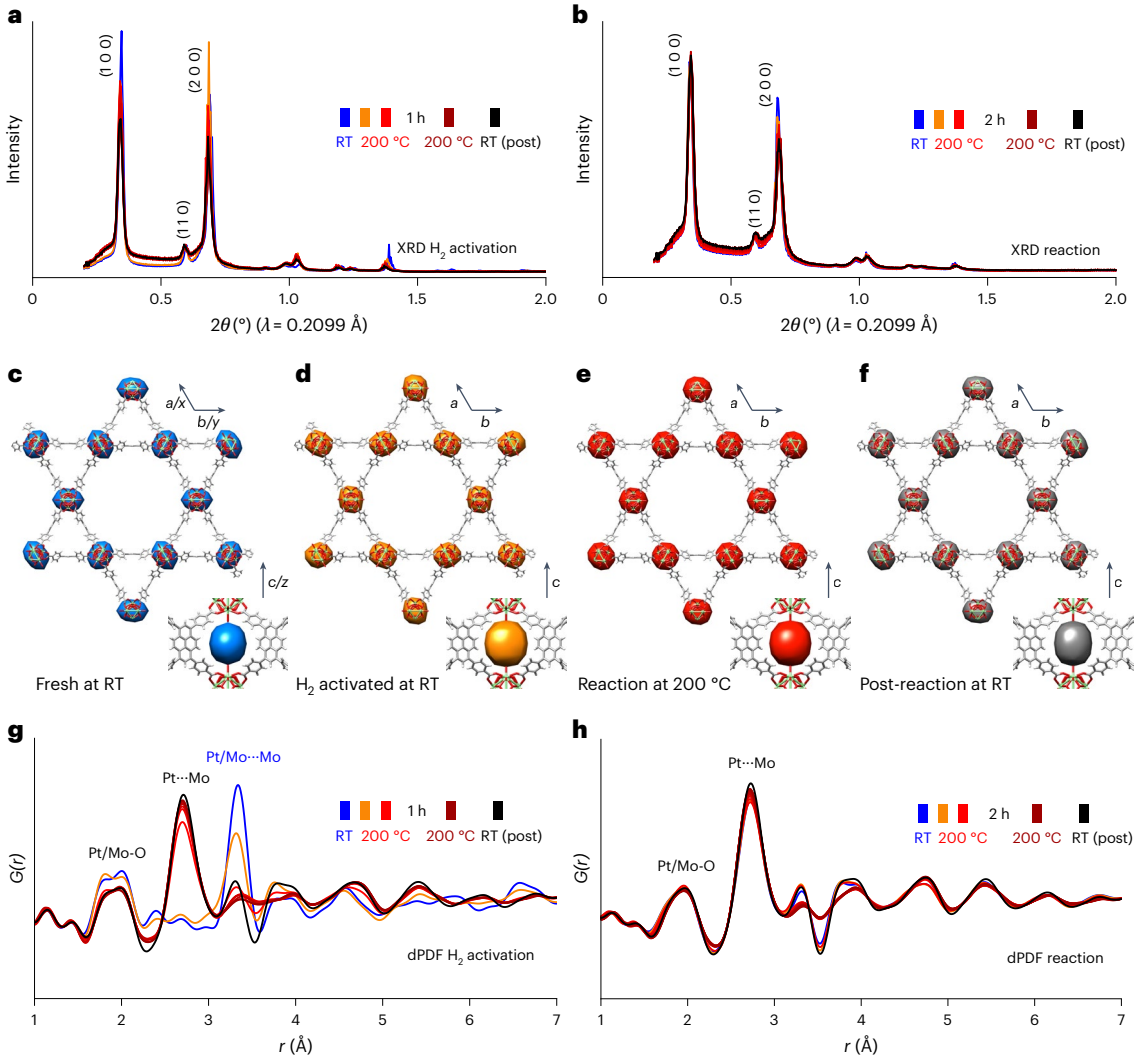

Fig. 2 | In situ X-ray scattering characterization of $PtMo_6O_{24}$@NU1K during H_2 activation and reaction conditions. a,**b**, Crystallinity and topology evolution of $PtMo_6O_{24}$@NU1K monitored by in situ XRD during a temperature cycle (room temperature → 200 °C → room temperature) under H_2 activation (**a**) and reaction conditions (**b**). **c**–**f**, The location of the $PtMo_6O_{24}$ clusters within the NU1K framework revealed by the DED of a fresh sample (**c**), H_2 activation (**d**), reaction conditions at 200 °C (**e**) and post-reaction (**f**). **g**,**h**, The local structural evolution of the isolated $PtMo_6O_{24}$ cluster confined in the *c*-pore of NU1K tracked by in situ dPDF during H_2 activation (**g**) and reaction (**h**), with a temperature ramp from room temperature to 200 °C and back. RT, room temperature.

In summary, the NU1K material possesses a mesoporous structure that can facilitate efficient mass transfer of reactant and product molecules. Its *c*-type pores not only stably confine the $PtMo_6O_{24}$ single clusters (8.6 Å × 7.8 Å × 3.1 Å), preventing their aggregation during the reaction process, but also provide accessible active interfaces for reactant molecules (Supplementary Fig. 28 and Supplementary Table 2). Furthermore, NU1K(Zr) can be easily synthesized on a large scale[30]. These advantages collectively make NU1K(Zr) an ideal support for confining $PtMo_6O_{24}$ single clusters.

Structure and active sites identification

Powder X-ray diffraction (PXRD) and pair distribution function (PDF) analyses confirmed that $PtMo_6O_{24}$ was successfully incorporated into the *c*-pores of NU1K without disrupting the long-range order of the framework (Fig. 2a,c, Supplementary Fig. 1 and Supplementary Fig. 41), consistent with previous reports[10]. During ramping of H_2 activation, relative peak intensities in PXRD changed while the space group of NU1K (*P6*/*mmm*) was retained (Fig. 2a). The difference envelope density (DED) maps indicated that the location of the $PtMo_6O_{24}$ clusters within the *c*-pores remained unchanged (Fig. 2d). Differential PDF (dPDF), obtained by subtracting the PDF of NU1K from that of $PtMo_6O_{24}$@NU1K at corresponding temperatures, revealed local structural changes associated with $PtMo_6O_{24}$ (Supplementary Fig. 1). Specifically, the intense peak at ~3.3 Å, attributed to metal…metal distances within the $PtMo_6O_{24}$, decreased in intensity, while a peak emerged at ~2.7 Å ($PtMo_6O_{24}$-R). This shorter metal…metal distance is below the known bond lengths of metallic Pt or Mo. At the same time, the peak intensity associated with metal–oxygen distances decreased, indicating partial reduction of the metal–oxygen bonds. During the dwelling, there was increased peak intensity at 2.7 Å in dPDFs (Fig. 2g and Supplementary Figs. 42a and 43a).

During CO_2 hydrogenation, the PXRD, DED and dPDFs results consistently suggested that both structures of the $PtMo_6O_{24}$-R clusters and the NU1K framework were structurally stable. No phase transformations or different crystalline phases were observed in PXRD (Fig. 2b). DED showed that $PtMo_6O_{24}$-R continued to be located within the *c*-pores (Fig. 2e,f), with no evidence of cluster migration/leaking or aggregation under catalytic reaction conditions. The dPDFs showed no notable changes other than an increase in the peak intensity at 2.7 Å (Fig. 2h). Variations from 3.0 to 3.7 Å were attributed to reversible structural changes of the NU1K reference PDFs at different temperatures (Supplementary Figs. 42b and 43b).

https://doi.org/10.1038/s41557-026-02104-x

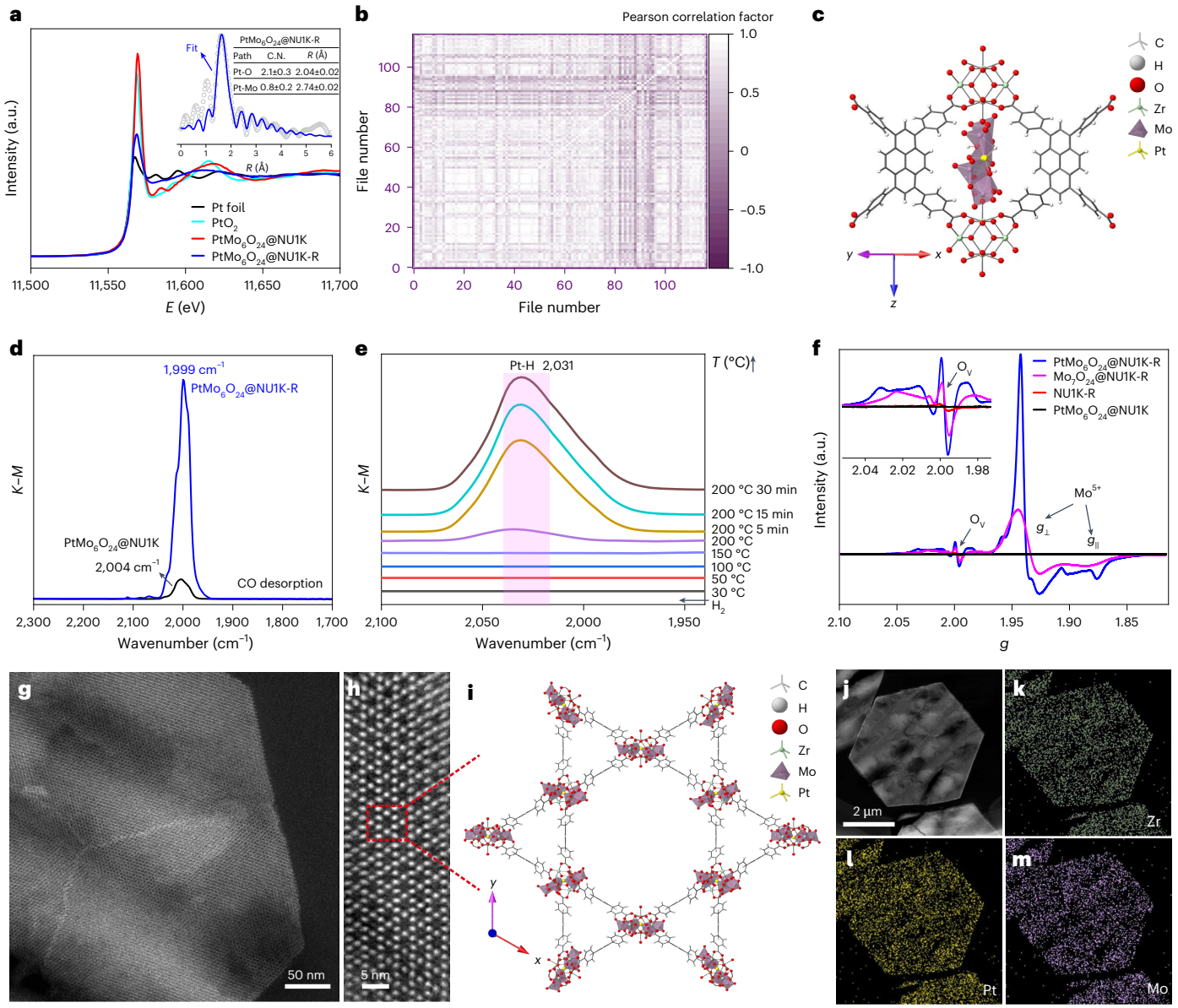

Fig. 3 | Microstructure characterization of the fresh and reduced $PtMo_6O_{24}$@NU1K catalyst. a, XANES (Pt) gives the oxidation state. The inset shows fitting curve and parameters for EXAFS data at the Pt L_3-edge for $PtMo_6O_{24}$@NU1K-R. **b**, A Pearson correlation matrix for the simulated PDFs and experimental dPDFs identifies the most promising candidates for further analysis. **c**, The location and atomic structure of $PtMo_6O_{24}$@NU1K-R clusters were determined based on in situ DED, dPDF and XAFS analyses. **d**, CO-DRIFTS of two samples retain the CO adsorption mode observed in the DRIFTS. K–M, the Kubelka–Munk function. **e**, In situ DRIFTS of H_2 activation on $PtMo_6O_{24}$@NU1K were recorded at different temperatures (*T*). **f**, EPR investigation of activated $PtMo_6O_{24}$@NU1K catalyst, NU1K, Mo_7O_{24}@NU1K and fresh samples. The inset shows an enlarged view of the O_V region in **f** to highlight the microscopic features. **g**–**i**, Different magnification (50 nm (**g**) and 5 nm (**h**)) Cs-corrected high-angle annular dark-field-STEM images of $PtMo_6O_{24}$@NU1K viewing along the *c*-axis, showing that the $PtMo_6O_{24}$ clusters are precisely encapsulated in the *c*-pores of NU1K, with the corresponding atomic model (**i**) from the dashed-red frame in **h**. **j**–**m**, EDS mapping of $PtMo_6O_{24}$@NU1K (**j**), indicating a homogeneous distribution of zirconium (**k**), platinum (**l**) and molybdenum (**m**). K–M, Kubelka–Munk function.

In situ X-ray absorption spectroscopy (XAS) was used to track catalyst structural changes during H_2 activation. Normalized X-ray absorption near-edge spectroscopy (XANES) plots showed that the white-line intensity of $PtMo_6O_{24}$@NU1K-R is between Pt foil and PtO_2 (Fig. 3a), which indicated that the valence of Pt in $PtMo_6O_{24}$@NU1K-R is lower than +4. The extended X-ray absorption fine spectroscopy (EXAFS) analysis for the central Pt showed that the coordination number of the first Pt–O shell decreased markedly and the Pt···Mo/O peak at ~3.3 Å disappeared (Supplementary Figs. 44 and 45). EXAFS curve fittings showed that the coordination numbers of Pt–O decreased substantially from 6.0 to 2.0 after H_2 reduction. The more rapid decline in the amplitude of k^2-weighted oscillations in the high *k* range (~8 to 12 $Å^{-1}$) of $PtMo_6O_{24}$@NU1K-R (Supplementary Fig. 46) also implied a pronounced decrease in coordination of the Pt. Notably, a peak corresponding to Pt–Mo bonds appears at ~2.74 Å. The results of EXAFS fitting data are summarized in Supplementary Table 4, which provides parameters for subsequent density functional theory (DFT) modelling. DFT calculations used Gaussian16 to simulate the structural transformation by adding hydrogen atoms to $PtMo_6O_{24}$ and then calculating the relaxed geometries[31] (see 'Computational details and DFT calculations' section in the Methods). Screening of 115 computationally simulated models against experimental PDF and XAS data for $PtMo_6O_{24}$@NU1K-R (Fig. 3b) were performed to assess the structural changes during reaction. Among them, the file that gave the best match (Supplementary Fig. 47,

file 88) was used to assess the reaction network. Among different models, shorter Pt–Mo distances were consistently observed when μ_3-O were removed (as water; Supplementary Fig. 47). In these models, the Pt coordination changes from six-coordinate octahedral PtO_6 to two-coordinate PtO_2, a geometry that provides open sites for binding gas molecules. Earlier spectroscopic characterizations and DFT calculations confirm that when activated under a reducing atmosphere, the central Pt site protruded from the Mo_6 ring, leaving it more exposed, with a lower coordination number. Combining comprehensive in situ synchrotron radiation characterizations with theoretical modelling, we have successfully reconstructed the atomic structure of the $PtMo_6O_{24}$ cluster confined in the *c*-pores of NU1K under reaction conditions (Fig. 3c), which is essential for elucidating the reaction mechanism and establishing structure–activity relationships.

CO adsorption DRIFTS of the $PtMo_6O_{24}$@NU1K showed a single peak near 2,004 cm^{-1} (Fig. 3d and Supplementary Fig. 48), assigned to CO linearly adsorbed on isolated cationic Pt. The peak shifted towards lower wavenumber at 1,999 cm^{-1} after reduction[32], with a marked increase in intensity (Fig. 3d and Supplementary Fig. 48). The CO-DRIFTS results confirmed the preservation of isolated Pt sites, with the exposed sites facilitating CO adsorption, consistent with the XANES and EXAFS results. To investigate the H_2 activation process, in situ DRIFTS were collected at temperatures from 30 °C to 200 °C under ambient 10% H_2/Ar flow conditions. As shown in Supplementary Fig. 49, a series of infrared bands at 3,600 cm^{-1} corresponding to different stretching vibrations of hydroxyls could be observed upon H_2 activation at 200 °C, demonstrating the combination of protons with O atoms[33]. Meanwhile, a single peak at 2,031 cm^{-1} corresponding to a Pt-hydride vibration was captured[34], providing strong evidence for heterolytic dissociation of H_2. That is, H_2 undergoes heterolytic dissociation induced by $Pt^{\delta+}$ and spills over to the surrounding μ_3-O atoms in $PtMo_6O_{24}$, generating O–H and Pt-hydride species (Fig. 3e). After sample heating in H_2 at 200 °C for an hour, the Pt-hydride vibration intensity decreased as the temperature decreased (but still observable) at room temperature as shown in Supplementary Fig. 50. The intensity decrease implies that the activation of H_2 on the $PtMo_6O_{24}$@NU1K catalyst is reversible. Electron paramagnetic resonance (EPR) spectra were employed to investigate the active sites for CO_2 activation. As shown in Fig. 3f, two types of EPR signals appeared on $PtMo_6O_{24}$@NU1K-R. One is assigned to the Mo^{5+} ions with a broad axial resonance at $g_\perp = 1.9378$ and $g_\parallel = 1.8758$ (ref. 35), the other sharp and nearly symmetric resonance is due to a free electron trapped in oxygen vacancies (O_V) at $g = 1.9973$ (ref. 33). Vacancies are anticipated based on net extraction of neutral oxygen by H_2 to form water, leaving behind two electrons per extracted atom. The role of oxygen vacancies is probably to trap the CO_2 molecule. We speculate that the CO_2 molecule is activated by electron transfer from $Pt^{\delta+}$ and Mo^{5+}. If the central Mo in the Mo_7O_{24} cluster is replaced with Pt, the concentrations of oxygen vacancies and Mo^{5+} in $PtMo_6O_{24}$@NU1K increase markedly compared with Mo_7O_{24}@NU1K. We attribute the increase to accelerated hydrogen dissociation on $Pt^{\delta+}$ and to hydrogen spillover to the nearest μ_3-O and peripheral Mo_6O_x nanorings[36].

To observe the interior structure, ultramicrotomy was used to slice the microcrystals thinly (~70 nm), facilitating the alignment of the structure along the [001] direction. Given that the reduced and post-reaction samples are highly reactive in air (with observed sparking or combustion phenomenon) and that the ultrathin slicing process inevitably involves exposure to moisture, these factors may all lead to changes in the sample structure. To accurately analyse the position of the clusters in NU1K, we used fresh samples for slicing and analysis. Typical STEM and enlarged images of $PtMo_6O_{24}$@NU1K acquired along the [001] direction are shown in Fig. 3g,h and Supplementary Fig. 51. The high-resolution images clearly display the ordered structure of NU1K, revealing its characteristic hexagonal channels (31 Å) and smaller trigonal channels (12 Å) in certain regions. Notably, the empty hexagonal and triangular channels in Fig. 3h confirm that the clusters are exclusively located within the *c*-pores rather than residing in the *ab*-plane channels, with the Pt atom of the disc-shaped cluster being accessible from both the mesopore and the micropore, which aligns with the DED data in Fig. 2c. The corresponding atomic model of $PtMo_6O_{24}$@NU1K-R from the dashed-red frame in Fig. 3h was fabricated in Fig. 3i based on earlier characterizations[37]. Energy-dispersive spectroscopy (EDS) mapping detected signals of platinum and molybdenum elements in the imaged area, with spatial distributions matching well with that of zirconium (Fig. 3j–m). These suggest uniform dispersion and isolation of the $PtMo_6O_{24}$ cluster in *c*-pores throughout the crystal.

In situ DRIFTS measurements (Fig. 4a) were used to track the evolution of reaction intermediates during CO_2 hydrogenation. When the reaction gas (CO_2:H_2 = 1:3) was introduced into a $PtMo_6O_{24}$@NU1K-R sample, CO* and CH_3O* species (with the asterisk indicating the adsorbed state) were observed. The peak at 1,999 cm^{-1} is assigned to linearly adsorbed CO*, while the peak at 2,035 cm^{-1} is assigned a Pt-hydride vibration. The peaks at 1,032, 2,859, 2,871, 2,905 and 2,941 cm^{-1} are attributed to a C–O stretching vibration ν(CO), C–H symmetric and C–H asymmetric stretching vibrations ν(CH) of CH_3O*, respectively[12,13]. The peak intensities increased with increasing temperature (Fig. 4a), implying that CO* and CH_3O* are intermediates in the catalytic hydrogenation of CO_2 to methanol. The time course of intermediate formation suggests that decomposition of CO_2 to CO* occurs first, followed by hydrogenation of CO* to form CH_3O*. The DRIFTS results (Fig. 4a) strongly suggest that CO_2 hydrogenation proceeds via the RWGS ($CO_2 + H_2 \rightarrow CO + H_2O$) and subsequent CO* hydrogenation (the RWGS + CO-hydro pathway)[38]. These results clearly demonstrate that CO_2 activation and hydrogenation occur over the $PtMo_6O_{24}$-R cluster, even under ambient pressure and room temperature conditions. When the pressure was increased to 1.5 MPa, DRIFTS intensities of all intermediate species increased over time. Among them, a peak at 2,745 cm^{-1} emerges, characteristic of the formate species (HCOO*)[39]; meanwhile, the amount of CO intermediates generated increases substantially, with its concentration exceeding that of the formate intermediates (Fig. 4a and Supplementary Fig. 52). Building on the work of Schlögl, Behrens and Studt regarding the competition between the CO* and HCOO* pathways on Cu[40–42], we used ^{13}C isotopic labelling and measured methanol formation rates under varying gas compositions to distinguish the dominant reaction mechanism. Isotopic labelling experiments were used to determine the CO* pathway during the reaction using $^{12}CO_2 + H_2$ and $^{12}CO_2 + {}^{13}CO + H_2$ as reaction gases, respectively. The gas chromatography–mass spectrometry experiments in Supplementary Fig. 53 show that $^{13}CH_3OH$ appeared when co-feeding ^{13}CO in reaction gas at reaction conditions, confirming the existence of the CO* pathway. Furthermore, the comparable methanol formation rates (36.2 and 43.2 μmol $g_{cat.}^{-1}$ min^{-1} at 200 °C in hydrogen from CO and CO_2, respectively) also suggests that CO is one direct source of methanol on $PtMo_6O_{24}$@NU1K-R catalyst[41] (Supplementary Fig. 54).

Reaction mechanism

DFT calculations were performed to study the underlying reaction mechanisms (Fig. 4b,c). CO_2 can chemisorb to oxygen-vacant sites between Pt and Mo, with carbon binding to Pt and oxygen to Mo. Next, CO_2 dissociates to CO* + O*. This step is thermodynamically and kinetically ($\Delta G^{\ddagger} = 1.25$ eV) more favourable than generation of either adsorbed carboxyl (COOH*) ($\Delta G^{\ddagger} = 1.47$ eV) or formate (HCOO*) ($\Delta G^{\ddagger} = 1.82$ eV) intermediates (Fig. 4b and Supplementary Figs. 55 and 56). The resulting O* is hydrogenated via hydride transfer from the Pt site to form OH*, which subsequently desorbs as H_2O through further hydrogenation. Desorption of CO* is unfavourable, with a desorption free energy of 2.76 eV, while hydrogenation of CO* to CHO* has a barrier of 1.49 eV. Thus, hydrogenation of CO is favoured over desorption (Fig. 4b). Hydrogenation of CO* to COH* is both kinetically ($\Delta G^{\ddagger} = 3.33$ eV) and thermodynamically less favourable than CHO* formation, further supporting CHO* as the preferred intermediate (Fig. 4b). Further hydrogenation

https://doi.org/10.1038/s41557-026-02104-x

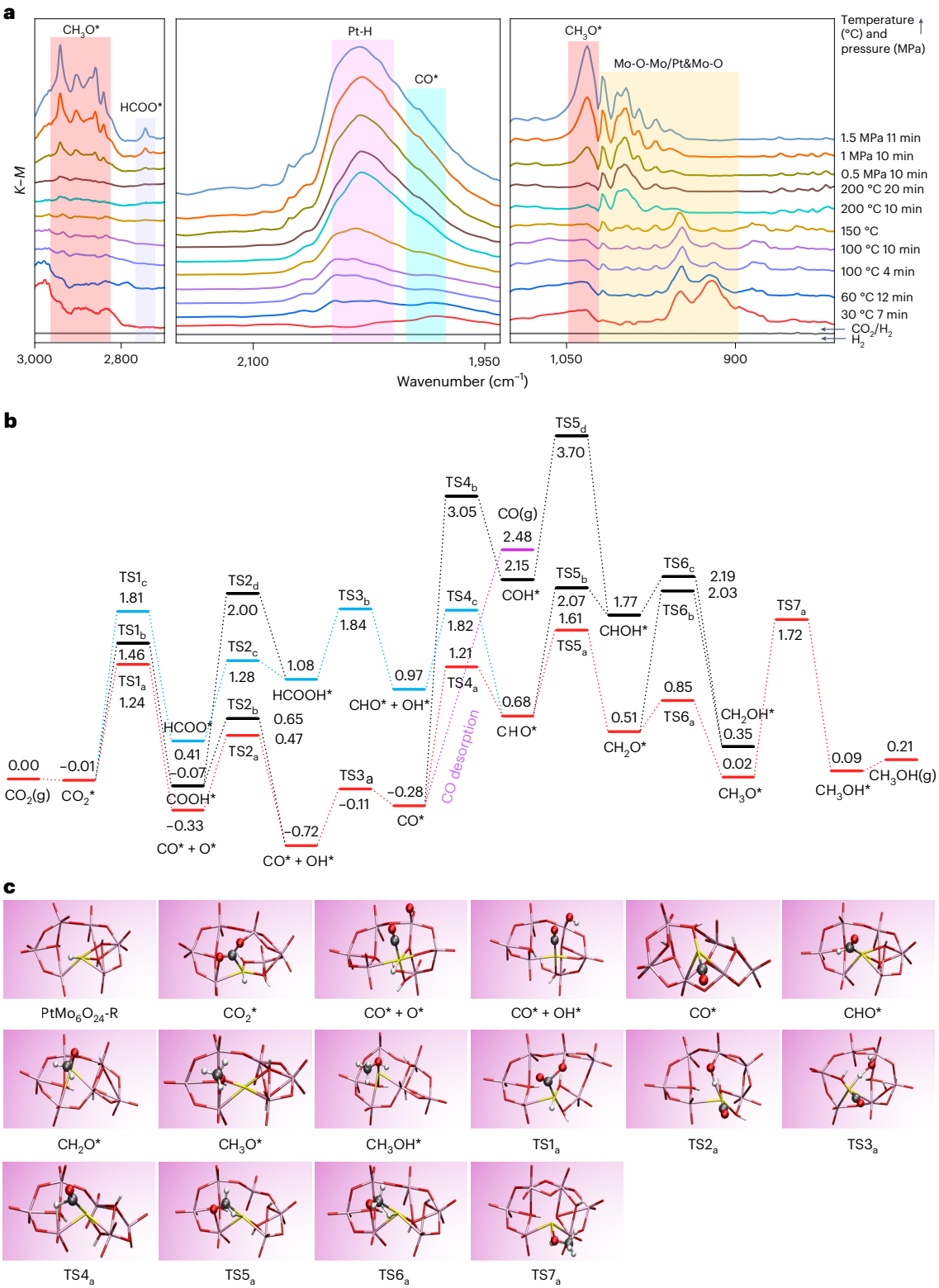

Fig. 4 | Study on the reaction mechanism of CO_2 hydrogenation to CH_3OH over $PtMo_6O_{24}$@NU1K. a, In situ DRIFTS of CO_2 hydrogenation over the $PtMo_6O_{24}$@NU1K catalyst under different reaction conditions. 'Mo-O-Mo/Pt &Mo-O' refers to the stretching vibrations of Mo-O-Pt, Mo-O-Mo and Mo-O bonds in $PtMo_6O_{24}$, derived from the $\{PtO_6\}$ and $\{MoO_6\}$ units. **b**, Gibbs Free-energy diagram (ΔG_{vib}) of CO_2 hydrogenation to CH_3OH over the reduced $PtMo_6O_{24}$@NU1K catalyst. The red line denotes the favourable pathway, while the blue line represents the formate pathway that converges with the main route via the CHO* intermediate. **c**, Structural diagrams of the intermediates and transition states for each reaction step in the red line. Colour legend: Mo (purple), Pt (gold), O (red), C (grey) and H (white).

of CHO* to CH_3OH proceeds through CH_2O* and CH_3O* as intermediates, whose formation are thermodynamically and kinetically more favourable than the formation of CHOH* and CH_2OH* as intermediates (Fig. 4b). This finding supports the presence of CH_3O* intermediates in in situ DRIFTS. Overall, DFT calculations suggest that CO_2 hydrogenation to methanol primarily follows direct CO_2 dissociation (RWGS-like)

coupled with subsequent CO hydrogenation: CO_2* → CO* + O* → CO* + OH* → CO* → CHO* → CH_2O* → CH_3O* → CH_3OH* (Fig. 4b).

The emergence of a HCOO* intermediate at high temperature and pressure suggests a second pathway could become viable under those conditions. HCOO* forms owing to direct hydrogenation of CO_2*. DFT calculations indicate that CO_2* hydrogenation to COOH* is more favourable; however, the COOH* intermediate facilely connects to the RWGS pathway owing to a relatively low barrier ($\Delta G^{\ddagger}$ = 0.72 eV) for dissociation to CO* + OH* (Fig. 4b). This is in alignment with the observation of CO* species in in situ DRIFTS. On the other hand, HCOO* species that are formed would be converted to HCOOH* ($\Delta G^{\ddagger}$ = 0.87 eV), which then would be converted to CHO* + OH* ($\Delta G^{\ddagger}$ = 0.76 eV) before reconnecting main hydrogenation channel after OH* removal as water (Fig. 4b and Supplementary Fig. 57). These findings support the experimental observation of HCOO* as a stable catalyst intermediate: COOH* species readily dissociate to CO* + OH* and probably have low coverages, while higher energies in the formate pathway slows HCOO* conversion, leading to observation of unconverted HCOO* on the catalyst. Overall, the formate pathway is less competitive than the direct CO_2 dissociation and COOH* routes owing to the larger barrier to HCOO* formation ($\Delta G^{\ddagger}$ = 1.82 eV) that exceeds direct CO_2 dissociation and COOH* formation ($\Delta G^{\ddagger}$ = 1.25 eV and 1.47 eV, respectively). This finding supports the experimental finding that trace amounts of HCOO* only emerge in high temperature and pressure conditions.

Conclusion

The main products of CO_2 hydrogenation on Pt-based catalysts are widely reported to be CO and water[21,38,43], as also observed with our control catalyst $PtMo_6O_{24}/ZrO_2$, Pt@NU1K, PtV_9O_{28}@NU1K and PtW_6O_{24}@NU1K. By contrast, we find that well-defined $PtMo_6O_{24}$ clusters, when isolated and stabilized by Zr-MOF confinement, are catalytically competent for CO_2 hydrogenation to methanol. In situ spectroscopic measurements together with DFT calculations give clear picture of H_2-activated $PtMo_6O_{24}$-R. Notably, H_2 is heterolytically dissociated on isolated, single-atom Pt sites to produce Pt-hydride and -OH species; CO_2 is trapped by an oxygen vacancy and subsequently reacts with hydrogen species to form CO* and water. Two more cluster-initiated H_2 dissociation cycles provide the hydrides and protons needed to form CH_3OH*. At higher pressure and temperature, the HCOO* intermediate appeared. Combined with ^{13}C isotopic labelling and measured methanol formation rates suggest that CO_2 hydrogenation to methanol on the $PtMo_6O_{24}$@NU1K catalyst proceeds predominantly through the RWGS + CO-hydro pathway, with the HCOO* pathway acting as an auxiliary route that may occur under high temperature and pressure. The $PtMo_6O_{24}$@NU1K catalyst achieved per-pass yields ranging from 1.2% at 100 °C to 13.1% at 200 °C, exceeding that of the state-of-the-art catalysts under similar conditions. $PtMo_6O_{24}$@NU1K displayed excellent durability, that is no detectable loss in activity or selectivity over 3,600 h, making it a simple and promising model system. This discovery opens a frontier in catalyst development, not only for low-temperature methanol synthesis and CO_2 conversion reactions, but also for other reactions catalysed, electrocatalysed or photocatalysed by well-defined, molecular-scale inorganic clusters. The uniform isolation and stabilization of single heteroatoms (catalysts) with clusters that, in turn, are organized and stabilized as periodic arrays by crystalline MOFs promises to enable fundamental mechanistic investigations and to facilitate discovery of catalyst performance-relevant structure–activity relationships.

Online content

Any methods, additional references, Nature Portfolio reporting summaries, source data, extended data, supplementary information, acknowledgements, peer review information; details of author contributions and competing interests; and statements of data and code availability are available at https://doi.org/10.1038/s41557-026-02104-x.

References

1. Artz, J. et al. Sustainable conversion of carbon dioxide: an integrated review of catalysis and life cycle assessment. *Chem. Rev.* **118**, 434–504 (2018).
2. Ye, J. et al. Hydrogenation of CO_2 for sustainable fuel and chemical production. *Science* **387**, eadn9388 (2025).
3. Pacchioni, G. From CO_2 to methanol on Cu/ZnO/Al_2O_3 industrial catalyst. What do we know about the active phase and the reaction mechanism?. *ACS Catal.* **14**, 2730–2745 (2024).
4. Cannizzaro, F., Hensen, J. M. E. & Filot, A. W. I. The promoting role of Ni on In_2O_3 for CO_2 hydrogenation to methanol. *ACS Catal.* **13**, 1875–1892 (2023).
5. Araújo, P. T. et al. Reaction-induced metal–metal oxide interactions in Pd-In_2O_3/ZrO_2 catalysts drive selective and stable CO_2 hydrogenation to methanol. *Angew. Chem. Int. Ed.* **62**, e202306563 (2023).
6. Amann, P. et al. The state of zinc in methanol synthesis over a Zn/ZnO/Cu(211) model catalyst. *Science* **376**, 603–608 (2022).
7. Kattel, S., Ramírez, J. P., Chen, G. J., Rodriguez, A. J. & Liu, P. Active sites for CO_2 hydrogenation to methanol on Cu/ZnO catalysts. *Science* **355**, 1296–1299 (2017).
8. Wang, K.-Y. et al. Bioinspired framework catalysts: from enzyme immobilization to biomimetic catalysis. *Chem. Rev.* **123**, 5347–5420 (2023).
9. Wang, S. et al. H_2-reduced phosphomolybdate promotes room-temperature aerobic oxidation of methane to methanol. *Nat. Catal.* **6**, 895–905 (2023).
10. Chen, Z. et al. Atomically precise single-site catalysts via exsolution in a polyoxometalate–metal–organic-framework architecture. *J. Am. Chem. Soc.* **146**, 7950–7955 (2024).
11. Bucior, B. J. et al. Identification schemes for metal–organic frameworks to enable rapid search and cheminformatics analysis. *Cryst. Growth Des.* **19**, 6682–6697 (2019).
12. Hu, J. et al. Sulfur vacancy-rich MoS_2 as a catalyst for the hydrogenation of CO_2 to methanol. *Nat. Catal.* **4**, 242–250 (2021).
13. Sugiyama, H., Miyazaki, M., Sasase, M., Kitano, M. & Hosono, H. Room-temperature CO_2 hydrogenation to methanol over air-stable hcp-PdMo intermetallic catalyst. *J. Am. Chem. Soc.* **145**, 9410–9416 (2023).
14. Bansode, A., Tidona, B., von Rohr, P. R. & Urakawa, A. Impact of K and Ba promoters on CO_2 hydrogenation over Cu/Al_2O_3 catalysts at high pressure. *Catal. Sci. Technol.* **3**, 767–778 (2013).
15. Koh, M. K., Khavarian, M., Chai, S. P. & Mohamed, A. R. The morphological impact of siliceous porous carriers on copper-catalysts for selective direct CO_2 hydrogenation to methanol. *Int. J. Hydrogen Energy* **43**, 9334–9342 (2018).
16. Xiao, S. et al. Highly efficient Cu-based catalysts via hydrotalcite-like precursors for CO_2 hydrogenation to methanol. *Catal. Today* **281**, 327–336 (2017).
17. Ahmad, K. & Upadhyayula, S. Conversion of the greenhouse gas CO_2 to methanol over supported intermetallic Ga–Ni catalysts at atmospheric pressure: thermodynamic modeling and experimental study. *Sustain. Energ. Fuels* **3**, 2509–2520 (2019).
18. Rungtaweevoranit, B. et al. Copper nanocrystals encapsulated in Zr-based metal–organic frameworks for highly selective CO_2 hydrogenation to methanol. *Nano Lett.* **16**, 7645–7649 (2016).
19. Wang, J., Lu, S. M., Li, J. & Li, C. A remarkable difference in CO_2 hydrogenation to methanol on Pd nanoparticles supported inside and outside of carbon nanotubes. *Chem. Commun.* **51**, 17615–17618 (2015).
20. Liu, G. et al. COx hydrogenation to methanol and other hydrocarbons under mild conditions with Mo_3S_4@ZSM-5. *Nat. Commun.* **14**, 513–523 (2023).

21. Gutterød, E. S. et al. Hydrogenation of CO_2 to methanol by Pt nanoparticles encapsulated in UiO-67: deciphering the role of the metal–organic framework. *J. Am. Chem. Soc.* **142**, 999–1009 (2019).
22. Zhu, Y. et al. Formation of (Rh-Fe)–FeO_x complex sites enables methanol synthesis from CO_2. *ACS Catal.* **14**, 10031–10039 (2024).
23. Lee, U. et al. Facile Incorporation of platinum(IV) into polyoxometalate frameworks: preparation of $[H_2Pt^{IV}V_9O_{28}]^{5-}$ and characterization by ^{195}Pt NMR spectroscopy. *Angew. Chem. Int. Ed.* **47**, 793–796 (2008).
24. Yu, F. et al. Pt-O bond as an active site superior to Pt° in hydrogen evolution reaction. *Nat. Commun.* **11**, 490 (2020).
25. Yu, H. et al. Transition-metal-controlled inorganic ligand-supported non-precious metal catalysts for the aerobic oxidation of amines to imines. *Chem. Eur. J.* **23**, 13883–13887 (2017).
26. Nomna, K., Takahashi, T., Shirai, T. & Miwa, M. Anderson-type heteropolyanions of molybdenum (VI) and tungsten (VI). *Polyhedron* **6**, 213–218 (1987).
27. Garibay, J. S., Iordanov, I., Islamoglu, T., DeCoste, B. J. & Farha, K. O. Synthesis and functionalization of phase-pure NU- 901 for enhanced CO_2 adsorption: the influence of a zirconium salt and modulator on the topology and phase purity. *CrystEngComm* **20**, 7066–7070 (2018).
28. Wang, R., Shi, K., Liu, J., Snurr, Q. R. & Hupp, T. J. Water-accelerated transport: vapor-phase nerve agent simulant delivery within a catalytic zirconium metal–organic framework as a function of relative humidity. *J. Am. Chem. Soc.* **145**, 13979–13988 (2023).
29. Beyzavi, H. et al. A hafnium-based metal-organic framework as an efficient and multifunctional catalyst for facile CO_2 fixation and regioselective and enantioretentive epoxide activation. *J. Am. Chem. Soc.* **136**, 15861–15864 (2014).
30. Wang, T. C. et al. Scalable synthesis and post-modification of a mesoporous metal-organic framework called NU-1000. *Nat. Protoc.* **11**, 149–162 (2016).
31. Frisch, M. J. et al. Gaussian 16 Revision C.02 (Gaussian Inc., 2019).
32. Li, X. et al. Functional CeO*x* nanoglues for robust atomically dispersed catalysts. *Nature* **611**, 284–288 (2022).
33. Feng, H. et al. Insights into bimetallic oxide synergy during carbon dioxide hydrogenation to methanol and dimethyl ether over GaZrO*x* oxide catalysts. *ACS Catal.* **11**, 4704–4711 (2021).
34. Deng, X. et al. Zeolite-encaged isolated platinum ions enable heterolytic dihydrogen activation and selective hydrogenations. *J. Am. Chem. Soc.* **43**, 20898–20906 (2021).
35. Gonzalez, R. J., Alcantara, R., Tirado, L. J., Fielding, J. A. & Dryfe, A. W. R. Electrochemical interaction of few-layer molybdenum disulfide composites vs sodium: new insights on the reaction mechanism. *Chem. Mater.* **29**, 5886–5895 (2017).
36. Liu, X. et al. Regulation of the properties of hydrogen dissociation and transfer in the presence of S atoms for efficient hydrogenations. *ACS Catal.* **14**, 16214–16223 (2024).
37. Aulakh, D. et al. Direct imaging of isolated single-molecule magnets in metal–organic frameworks. *J. Am. Chem. Soc.* **141**, 2997–3005 (2019).
38. Zhao, H., Liu, X., Zeng, C., Liu, W. & Tan, L. Thermochemical CO_2 reduction to methanol over metal-based single-atom catalysts (SACs): outlook and challenges for developments. *J. Am. Chem. Soc.* **146**, 23649–23662 (2024).
39. Lu, Z. et al. Node-accessible zirconium MOFs. *J. Am. Chem. Soc.* **142**, 21110–21121 (2020).
40. Studt, F. et al. The mechanism of CO and CO_2 hydrogenation to methanol over Cu-based catalysts. *ChemCatChem* **7**, 1105–1111 (2015).
41. Kunkes, E. L., Studt, F., Abild-Pedersen, F., Schlögl, R. & Behrens, M. Hydrogenation of CO_2 to methanol and CO on Cu/ZnO/Al_2O_3: is there a common intermediate or not?. *J. Catal.* **328**, 43–48 (2015).
42. Sha, F., Han, Z., Tang, S., Wang, J. & Li, C. Hydrogenation of carbon dioxide to methanol over non-Cu-based heterogeneous catalysts. *ChemSusChem* **13**, 6160–6181 (2020).
43. Jiang, X., Nie, X., Guo, X., Song, C. & Chen, J. G. Recent advances in carbon dioxide hydrogenation to methanol via heterogeneous catalysis. *Chem. Rev.* **120**, 7984–8034 (2022).

Methods

Chemical and materials

Disodium hexahydroxoplatinate ($Na_2Pt(OH)_6$), sodium molybdate dihydrate ($Na_2MoO_4{\cdot}2H_2O$), ammonium molybdate tetrahydrate ($(NH_4)_6M_7O_{24}{\cdot}4H_2O$), zirconium oxychloride octahydrate ($ZrOCl_2{\cdot}8H_2O$), chloroplatinic acid hexahydrate ($H_2PtCl_6{\cdot}6H_2O$), zirconium dioxide (ZrO_2), benzoic acid, dimethlyformamide (DMF), trifluoroacetic acid (TFA), solvents and reagents were purchased from Sigma-Aldrich with a purity more than 99%, and were used without further purification. Ultrapure deionized water (18.2 MΩ cm resistivity) was obtained from a Millipore Milli-Q Biocel A10 instrument (Millipore). All gases used for the adsorption and desorption measurements were of ultrahigh-purity grade 5 and were obtained from Airgas Specialty Gases. All solutions used in experiments were prepared with ultrapure deionized water.

Catalyst preparation

Synthesis of $Na_2[H_6PtMo_6O_{24}]{\cdot}29H_2O$ (abbreviated as $PtMo_6O_{24}$). The $PtMo_6O_{24}$ was synthesized according to the synthesis method reported in our previous literature[10]. Light-yellow platinum crystals were obtained from a mixed aqueous solution containing $Na_2Pt(OH)_6$ and $Na_2MoO_4{\cdot}2H_2O$. Then 0.7328 g $Na_2MoO_4{\cdot}2H_2O$ was dissolved in 5 ml H_2O and 0.1732 g $Na_2Pt(OH)_6$ was dissolved in 10 ml H_2O. Then these two solutions were mixed and stirred for 30 min. Crystallization began after adjusting the pH to 1.8 using 1 mol l^{-1} HNO_3. Crystals were collected via vacuum filtration.

NU1K synthesis. First, 4.85 g $ZrOCl_2{\cdot}8H_2O$ and 100 g benzoic acid were mixed in 300 ml of DMF in a glass bottle and ultrasonically dissolved. The clear solution was incubated in an oven at 100 °C for 1 h. In the meantime, 2 g H_4TBAPy was added to 100 ml DMF and heated to 100 °C for 1 h. After cooling down to room temperature, the H_4TBAPy solution and 2 ml TFA were added to premade Zr node containing solution and sonicated for 20 min. The yellow suspension was placed in a preheated oven at 120 °C for overnight (18 h). After cooling down to room temperature, the yellow powder material was washed with DMF three times and soaked for about 1 h between washes. To remove the coordinated modulator (benzoic acid) from the node, an HCl washing step was performed as follows. The resulting yellow powder was suspended in 650 ml DMF in a glass bottle and 25 ml of 8 M aqueous HCl was added. This mixture was heated in an oven at 100 °C overnight. After cooling to room temperature, the powder was washed with DMF three times and acetone three times (soaked for ~1 h between washes) and soaked in acetone overnight. NU1K powder was collected by centrifugation and dried in a vacuum desiccator and then activated at Micromeritics Smart VacPrep instrument as described later (yield of ~2.8 g activated NU1K).

Synthesis of $PtMo_6O_{24}$@NU1K. In a centrifuge tube, 137 mg $PtMo_6O_{24}$ was dissolved in 10 ml of deionized water. To the solution, 50 mg NU1K was added and suspended by sonicating for about 1 min. The suspension was shaken periodically or stirred. After 3 days, the solid was washed with water two times. Then the solid was washed with acetone three times. $PtMo_6O_{24}$@NU1K was allowed to soak in acetone overnight to ensure adequate removal of water. The yellowish target product was obtained after drying in a vacuum desiccator before activation on the Smart VacPrep. The solid material was subjected to inductively coupled plasma optical emission spectroscopy (ICP-OES) to determine the final POM loading Supplementary Table 1.

Synthesis of $PtMo_6O_{24}/ZrO_2$. $PtMo_6O_{24}$@ZrO_2 was prepared by incipient wetness impregnation. The Pt loading content in $PtMo_6O_{24}/ZrO_2$ was comparable to that of $PtMo_6O_{24}$@NU1K, as determined by ICP-OES analysis.

Synthesis of Pt@NU1K. Pt nanoparticles were synthesized according to a modified literature method[44]. The H_2PtCl_6 solution (6.0 mM) was prepared through dissolution of $H_2PtCl_6{\cdot}6H_2O$ in ultrapure water. Then 16.6 mg of PVP (molecular weight of 55,000) was dissolved in 45 ml of ethanol and 5.0 ml of a 6.0 mM H_2PtCl_6 solution was added dropwise. After stirring for approximately 10 min at room temperature, the mixture was refluxed for 3 h under air to form the PVP-stabilized Pt nanoparticles. Next, 80 mg of NU1K powder was added to the solution under vigorous stirring at room temperature for 3 h. The resulting Pt@NU1K was then collected by centrifugation at 5,017*g* for 10 min and washed three times with ethanol. Finally, the Pt@NU1K powders were dried at room temperature in a vacuum oven.

Catalyst characterizations

XRD analysis. PXRD measurements were performed at the IMSERC X-ray Facility (Northwestern University) using a STOE-STADI-MP diffractometer configured with an asymmetric curved Ge (111) monochromator for Cu $K\alpha_1$ radiation (λ = 1.54056 Å), a MYTHEN2 1 K silicon strip detector (DECTRIS) and a line-focused Cu X-ray source operating at 40 kV/40 mA. Sample preparation involved packing the powder in a 3-mm stainless steel sample holder with polyimide tape windows. Data were collected in the 2–20° 2θ range with 5–10 min exposure time. Instrument calibration was verified using NIST Silicon standard reference material 640 days before measurements.

Sorption studies. N_2 adsorptio–desorption isotherms were acquired at 77 K using a Micromeritics TriStar II 3020 surface area analyser (Micromeritics Instrument Corp.). Before measurements, approximately 40 mg of each sample was degassed at 120 °C for 24 h under dynamic vacuum (<10 μm Hg) using a Micromeritics Smart VacPrep preparation station. The Brunauer–Emmett–Teller specific surface area was calculated from the adsorption branch in the relative pressure range (P/P_0) of 0.005–0.05. Pore size distributions were derived from the adsorption isotherms using DFT calculations with a carbon slit-pore model and N_2 adsorption kernel at 77 K.

ICP-OES. Elemental analysis was performed using a Thermo Scientific iCAP 7600 ICP-AES system operating across the 166–847 nm spectral range. Samples (2–6 mg) were digested in 2–3 m concentrated HNO_3 (trace-metal grade, Fisher Scientific) with heating in a Biotage SPX microwave reactor (software version 2.3, build 6250) at 150 °C for 20 min. The digestate was diluted to 10–13 ml final volume with Milli-Q water (18.2 MΩ cm) and quantification was achieved by monitoring three/four emission lines per element: Pt (265.945, 214.423 and 203.646 nm), Mo (202.030, 204.598 and 203.844 nm), Zr (339.198, 343.823 and 327.305 nm), W (339.198, 343.823, 327.305 and 349.621 nm), V (310.23, 292.402, 290.882 and 309.311 nm), Zn (202.55, 206.19 and 213.86 nm) and Al (309.27, 396.15, 237.34 and 308.22 nm). Calibration utilized seven-point standard curves (1.563, 3.125, 6.25, 12.5, 25, 50 and 100 ppm) prepared from certified reference materials (high-purity standards) for each analyte.

The EPR spectra were acquired at room temperature using a JEOL JES-FA200 spectrometer. Before measurement, samples (NU1K, Mo_7O_{24}@NU1K and $PtMo_6O_{24}$@NU1K) were pretreated under 5% H_2/Ar flow at 200 °C for 1 h. After cooling to ambient temperature under reaction gas, the quartz reactor was sealed and transferred to an argon-filled glovebox (O_2 <0.1 ppm, H_2O <0.1 ppm). Samples were transferred under argon protection to quartz EPR tubes (4 mm optical density) and sealed. The operating conditions of the EPR spectrometer were as follows: microwave power 1 mW, γ-microwave frequency (MHz) and H-resonance field (mT)

$$g = 0.07145 \times \gamma(\mathrm{MHz})/\mathrm{H(mT)}.$$

High-angle annular dark-field-STEM images were recorded on a JEM ARM200F cold-field emission microscope equipped with a probe Cs-corrector operating at 200 kV. The MOF samples were loaded on Cu

microgrid (300 mesh) for imaging. The interior structure of MOF samples was prepared using a Leica ultramicrotome to slice 70-nm-thick slices with a Diatome diamond knife. The elemental composition and distribution were analysed by an energy-dispersive X-ray analyser (EX-230**BU EX-37001) mounted on the electron microscope. The crystalline structure was analysed using Gatan DigitalMicrograph software 3.53.4137.0.

In situ X-ray total scattering measurements. High-energy X-ray total scattering data (λ = 0.2115 Å) were acquired at beamline 11-ID-B for PDF analysis and at beamline 17-BM for DED analysis at the Advanced Photon Source (APS), Argonne National Laboratory. Powder samples of $PtMo_6O_{24}$@NU1K and NU1K were packed into a 1.0-mm ID quartz capillary mounted on a flow-cell reactor[45] to evaluate the structural changes during the H_2 activation and CO_2 hydrogenation to methanol. The samples were first heated to 200 °C in 20 sccm of 10% H_2 in He at ramp rate of ~10 °C min^{-1} and annealed for 1 h. After cooling to room temperature and purging with He, the samples were reheated to 200 °C in mixture of 18 sccm of H_2 and 6 sccm of CO_2 at the same ramp rate. Scattering data for PXRD and PDF analyses were collected at two different sample detector distances. Two-dimensional scattering images were reduced to one-dimensional data arrays using GSAS-II[46]. PDFs were extracted from the total scattering data with PDFgetX3 (refs. 47,48). The dPDFs were obtained by subtracting the reference PDF data of NU1K-formate free at 200 °C from that of $PtMo_6O_{24}$@NU1K using fityk[49,50]. Pawley refinements were performed in TOPAS7[51] to determine lattice parameters and peak intensities. The difference envelope densities were calculated by scaling and subtracting the structure envelopes of pristine, formate-free NU1K from $PtMo_6O_{24}$@NU1K under identical conditions[52] and visualized using Chimera[53].

Model screening based on the PDF data. The PDFs of computational models were simulated using Diffpy-CMI[54]. A Pearson correlation analysis[55] was applied to compare the similarity between the simulated PDFs of the models and the experimental dPDFs of the $PtMo_6O_{24}$-R sample. The range for the analysis was selected to be 1.5–5.0 Å.

In situ XAS measurements were conducted at beamline 5-ID-D using PIPS detectors at the APS, Argonne National Laboratory, in transmission mode at room temperature. XAS data were collected from room temperature to 200 °C under a 3.5% H_2/N_2 atmosphere. Spectra were recorded at the platinum L_3-edge (11,564 eV) and molybdenum K edge (20,000 eV) in transmission mode. The X-ray beam was monochromatized using a Si (111) monochromator and detuned by 15% to minimize higher-order harmonic contributions below the noise level. Metallic platinum and molybdenum foils were used as energy calibration references and were measured simultaneously with the experimental samples. PtO_2, $PtMo_6O_{24}$@NU1K and MoO_3 were analysed as reference samples. Data processing was performed using the Athena and Artemis programs within the IFEFFIT package, based on FEFF 6 (refs. 56,57). Before merging, spectra were calibrated against reference spectra, aligned to the first peak in the smoothed first derivative of the absorption spectrum, background noise was removed and spectra were normalized to obtain a unit edge step. XAS curve fitting of the Pt L_3-edge was conducted in the interatomic distance (R) space within an R range of 1.25–3.05 Å for k^2-weighted $\chi(k)$ functions, employing Hanning windows (dk = 1.0 $Å^{-1}$) and a k range of 2.65–10.55 $Å^{-1}$.

In situ DRIFTS measurements were performed on a Thermo Scientific Nicolet iS50 FTIR spectrometer equipped with a mercury–cadmium–telluride detector and a high-temperature cell with ZnSe windows. For the DRIFTS CO chemisorption measurement, after loading 20 mg sample into the cell, the sample was purged with Ar and a background spectrum was collected. Afterwards, 10% CO/Ar at a flow rate of 20 ml min^{-1} was introduced to the cell for 20 min to saturate the sample. Finally, the sample was purged with Ar at a flow of 20 ml min^{-1} for 30 min to remove the gas-phase CO, and a spectrum before reduction was collected with 16 scans at a resolution of 4 cm^{-1}. Then the sample was purged with Ar and reduced in 10% H_2/Ar at 200 °C. After cooling the sample to room temperature under Ar, a background spectrum was collected. Afterwards, 10% CO/Ar at a flow rate of 20 ml min^{-1} was introduced to the cell for 20 min to saturate the sample. Finally, the sample was purged with Ar at a flow of 20 ml min^{-1} for 30 min to remove the gas-phase CO, and a spectrum after reduction was collected with 16 scans at a resolution of 4 cm^{-1}. For the DRIFTS H_2 dissociation measurement, after loading fresh sample into the cell, the sample was purged with Ar, and a background spectrum was collected. Afterwards, 10% H_2/Ar at a flow rate of 20 ml min^{-1} was introduced to the cell with temperature gradually increased to 30 °C, 50 °C, 100 °C, 150 °C and 200 °C, during which the infrared spectra were continuously collected at each temperature with 16 scans at a resolution of 4 cm^{-1}. After a series of spectra were collected until the signals stabilized at 200 °C. The spectra were continuously collected at each temperature during the process of cooling from 200 °C to 150 °C, 100 °C, 50 °C and 30 °C.

In situ DRIFTS measurements during exposure to $CO_2 + H_2$ reaction gases were performed on a H_2-activated sample at different temperatures and pressures. The sample was first reduced in 10% H_2/Ar at 200 °C, 0.1 MPa for 1 h. Then a background spectrum was then collected after reduction step. The reaction gas (24% CO_2, 72% H_2 and 4% Ar) at a flow rate of 20 ml min^{-1} and 0.1 MPa was introduced to the sample for 50 min with temperature gradually increased to 30 °C, 60 °C, 100 °C, 150 °C and 200 °C, during which the infrared spectra were continuously collected at each temperature with 16 scans at a resolution of 4 cm^{-1}. Afterwards, a series of spectra were collected until the signals stabilized at 200 °C. Next, the pressure was gradually increased to 0.5 MPa, 1.0 MPa and 1.5 MPa, during which the infrared spectra were continuously collected at each pressure until it stabilized.

Isotopic labelling experiments. In the isotope experiment, a mixture of reaction gas and ^{13}C-labelled CO were co-fed in the ratio of $^{13}CO:CO_2:H_2$:Ar of 6:6:18:1. The reaction was conducted at 200 °C under a pressure of 1.5 MPa and the products were collected through an air bag and analysed using gas chromatography–mass spectrometry.

Catalyst performance evaluation

The catalytic performance for CO_2 hydrogenation was evaluated using a tubular fixed-bed continuous-flow reactor (Hefei In Situ Technology). In a typical reaction, 200 mg of catalyst diluted with 1.0 g of quartz sand was loaded into the reactor and reduced in 10% H_2/N_2 (0.1 MPa, 30 ml min^{-1}) at 200 °C for 1 h. After reduction, the reaction gas (24% CO_2, 72% H_2 and 4% Ar) was introduced into the reactor and pressurized to 5.0 MPa at room temperature. The temperature was raised to 200 °C and then decreased to room temperature, with a data measurement every 20 °C, running for 4 h at each temperature. The flow rate was adjusted to achieve the desired weight hourly space velocity. The outlet gas was analysed using an online gas chromatograph (Fuli GC9720Plus) equipped with thermal conductivity and flame ionization (FID) detectors. Porapak Q and 5A packed columns connected to the thermal conductivity detector were used to analyse CO, Ar and CO_2 products; whereas a PLOT Q capillary column connected to the flame ionization detector was used to analyse methane, methanol (MeOH), dimethyl ether (DME) and other products. The conversion of CO_2, selectivity, space–time yield (STY) and methanol yield—denoted as $C(CO_2)$, $S(CH_3OH)$, STY(CH_3OH) and $Y(CH_3OH)$—were calculated using equations (2)–(5), based on an internal normalization method described elsewhere[58]

$$F_{x,out} = \frac{C_{x,out} \times F_{Ar,in}}{C_{Ar,out}}, \quad (1)$$

$$C(CO_2) = \frac{F_{CO_2,in} - F_{CO_2,out}}{F_{CO_2,in}}, \quad (2)$$

$$S(CH_3OH) = \frac{F_{CH_3OH}}{2 \times F_{DME} + 2 \times F_{C_2H_4} + 2 \times F_{C_2H_6} + F_{CO} + F_{CH_4} + F_{CH_3OH}}, \quad (3)$$

$$STY(CH_3OH) = \frac{F_{CO_2,in} \times X(CO_2) \times S(CH_3OH)}{W} \times M(CH_3OH), \quad (4)$$

$$Y(CH_3OH) = C(CO_2) \times S(CH_3OH), \quad (5)$$

where F_i is molar flow rate of the product and reactant and W is the weight of catalyst sample.

The STY of MeOH was calculated according to equation (4) and was normalized by the catalyst mass ($g_{MeOH}\ kg_{cat.}^{-1}\ h^{-1}$), where M_{CH3OH} is the molar mass of methanol (32 g mol^{-1}). Note that all data points were collected after 4 h of reaction to ensure the catalyst reached steady state at each temperature.

Computational details and DFT calculations

Identification of the cluster structure after H_2 reduction of the $[PtMo_6O_{18}(OH)_6]^{2-}$ cluster model was performed systematically through sequential hydrogenation and dehydration steps. Specifically, starting from a $[PtMo_6O_{18}(OH)_6]^{2-}$ model, hydrogen atoms were introduced at oxide (O^{2-}), hydroxide (OH^-) and platinum sites, reflecting the likely reduction sites under H_2 and the structure was re-optimized. In cases where hydrogen added to μ_3-OH could form H_2O, the H_2O was removed and the structure was re-optimized again. A total of 115 candidate structures were evaluated. Both singlet and triplet spin states were considered during the geometry optimization process. All structures were screened against experimental dPDF data. Among these, the $H_4PtMo_6O_{20}$ cluster (Supplementary Fig. 47) showed the highest Pearson correlation (Fig. 3b) and reproduced key local structural features, including shorter metal–metal bond distances and lower coordination at Pt sites. Similar approaches have previously been used to identify the structure of H_2-reduced $[RhMo_6O_{18}(OH)_6]^{3-}$ clusters and to determine encapsulated species in both polyoxometalates and transition-metal sulfide clusters by matching simulated and experimental dPDFs[10,59,60]. The chemical composition of H_2 reduced modelled structures is as follows: (1) $H_8PtMo_6O_{24}$ species formed after the addition of H_2 in the $[PtMo_6O_{18}(OH)_6]^{2-}$ cluster, (2) $H_6PtMo_6O_{23}$ species formed after the removal of one H_2O from the $H_8PtMo_6O_{24}$ cluster species, (3) $H_4PtMo_6O_{22}$ species formed after the removal of two H_2O molecules from the $H_8PtMo_6O_{24}$ cluster species, (4) $H_6PtMo_6O_{22}$ species formed by the further reduction of $H_4PtMo_6O_{22}$ with H_2, (5) $H_4PtMo_6O_{21}$ species formed after the removal of one H_2O from the $H_6PtMo_6O_{22}$ cluster species, (6) $H_2PtMo_6O_{20}$ species formed after removal of two H_2O from the $H_6PtMo_6O_{22}$ cluster species, (7) $H_8PtMo_6O_{22}$ species formed by the further reduction of $H_6PtMo_6O_{22}$ with H_2 and (8) $H_4PtMo_6O_{20}$ species formed after the removal of two H_2O from the $H_8PtMo_6O_{22}$ cluster species. DFT calculations for the ten model structures exhibiting the best agreement with experimental dPDF data, including key intermediates and transition states along the CO_2 hydrogenation pathway, are available in the ioChem-BD repository[61,62] and can be accessed via ref. 63.

DFT calculations were carried out using the Gaussian16 program[31]. The geometries of all studied species were optimized in gas phase, mostly without geometric constraints, except for certain geometries where the Mo–Mo distances were held fixed to resemble geometric constraints inside the pore of MOF (Supplementary Fig. 47). The M06-L functional and the def2-TZVP basis set for all atomic centres were employed[64,65]. Relaxations were carried out using default convergence criteria in Gaussian16. The natures of all stationary points were confirmed by vibrational frequency analysis: minima exhibited no imaginary frequencies and transition states were verified as first-order saddle points with exactly one imaginary frequency. Gibbs free energies (ΔG, 298.15 K, 1 atm) were obtained from harmonic frequency calculations at the M06-L/def2-TZVP level of theory, including zero-point, enthalpic and entropic contributions.

Initial free energies obtained under the rigid-rotor–harmonic-oscillator (RRHO) approximation (G_{RRHO}) were refined using GoodVibes v3.2 to obtain quasi-harmonic free energies (G_{qh})[66]. A vibrational scale factor of 1.0 was used, and Grimme's quasi-harmonic scheme was applied with a 50 cm^{-1} cut off to damp the exaggerated entropic contributions from low-frequency modes by interpolating between harmonic and free-rotor limits[67]. All reported G_{qh} values were evaluated at 298.15 K and referenced to a 1 atm standard state.

As the underlying quantum-chemical calculations were performed on isolated gas-phase clusters, the resulting free-energy profiles represent upper bounds to the true thermodynamics under MOF confinement, where translational and rotational motion is strongly restricted[68]. To better approximate the confined pore environment, translational and rotational entropy contributions were neglected and only vibrational and electronic terms were retained when comparing intermediates and transition states (Fig. 4b and Supplementary Figs. 55–57). The vibrational-only free energies (G_{vib}) were evaluated with the same quasi-harmonic correction, ensuring low-frequency modes were treated consistently. At 298.15 K and referenced to the gas-phase standard state, ΔG_{vib} for the most part lie between ΔG_{qh} and the corresponding electronic energies, with the exception of a few reactions that occur on the catalyst, where ΔG_{vib} are lower than but within 0.12 eV of the electronic energies (Supplementary Fig. 58). This illustrates that ΔG_{vib} is a physically realistic middle ground.

M06-L is a meta-GGA functional that offers reliable performance for transition-metal chemistry and catalytic thermochemistry, with its suitability for CO_2 hydrogenation catalysis supported by prior studies[69,70]. In addition, M06-L has also been successfully applied in previous works to identify the structures of encapsulated polyoxo- and polythiolmetalate clusters[10,59,60]. We tested the sensitivity of the M06-L-calculated energetics by performing single-point energy evaluations with other functionals (M06, B3LYP and ωB97X-D) on the M06-L/def2-TZVP geometries for selected reaction steps[71–73] (Supplementary Table 5 and Supplementary Table 6). We find that the relative barriers and energetic preferences of the various pathways are not sensitive to the functional.

Data availability

All other data are available within the Article and its Supplementary Information and are also available from the corresponding author upon reasonable request. Source data are provided with this paper. MOFkey is as follows: HZr.HVCDAMXLLUJLQZ.MOFkey-v1.csq (NU-1000).

References

44. Zhao, M. et al. Metal-organic frameworks as selectivity regulators for hydrogenation reactions. *Nature* **539**, 76–80 (2016).
45. Chupas, P. J. et al. A versatile sample-environment cell for non-ambient X-ray scattering experiments. *J. Appl. Crystallogr.* **41**, 822–824 (2008).
46. Toby, B. H. & Von Dreele, R. B. GSAS-II: the genesis of a modern open-source all purpose crystallography software package. *J. Appl. Crystallogr.* **46**, 544–549 (2013).
47. Yang, Y., Juhas, P., Farrow, C. L. & Billinge, S. J. xPDFsuite: an end-to-end software solution for high throughput pair distribution function transformation, visualization and analysis. Preprint at https://arxiv.org/abs/1402.3163 (2015).
48. Juhas, P., Davis, T., Farrow, C. L. & Billinge, S. J. L. PDFgetX3: a rapid and highly automatable program for processing powder diffraction data into total scattering pair distribution functions. *J. Appl. Crystallogr.* **46**, 560–566 (2013).
49. Wojdyr, M. Fityk: a general-purpose peak fitting program. *J. Appl. Crystallogr.* **43**, 1126–1128 (2010).
50. Chen, Z. et al. Node distortion as a tunable mechanism for negative thermal expansion in metal–organic frameworks. *J. Am. Chem. Soc.* **145**, 268–276 (2023).

51. Coelho, A. TOPAS and TOPAS-Academic: an optimization program integrating computer algebra and crystallographic objects written in C++. *J. Appl. Crystallogr.* **51**, 210–218 (2018).
52. Yakovenko, A. A. et al. Study of guest molecules in metal–organic frameworks by powder X-ray diffraction: analysis of difference envelope density. *Cryst. Growth Des.* **14**, 5397–5407 (2014).
53. Pettersen, E. F. et al. UCSF ChimeraX: structure visualization for researchers, educators, and developers. *Protein Sci.* **30**, 70–82 (2021).
54. Juhas, P., Farrow, C. L., Yang, X., Knox, K. R. & Billinge, S. J. L. Complex modeling: a strategy and software program for combining multiple information sources to solve ill posed structure and nanostructure inverse problems. *Acta Crystallogr. A* **71**, 562–568 (2015).
55. O'Nolan, D. et al. A multimodal analytical toolkit to resolve correlated reaction pathways: the case of nanoparticle formation in zeolites. *Chem. Sci.* **12**, 13836–13847 (2021).
56. Rehr, J. J. & Albers, R. C. Theoretical approaches to X-ray absorption fine structure. *Rev. Mod. Phys.* **72**, 621–654 (2000).
57. Ravel, B. & Newville, M. ATHENA, ARTEMIS, HEPHAESTUS: data analysis for X-ray absorption spectroscopy using IFEFFIT. *J. Synchrotron Radiat.* **12**, 537–541 (2005).
58. Zhu, Y. et al. Copper–zirconia interfaces in UiO-66 enable selective catalytic hydrogenation of CO_2 to methanol. *Nat. Commun.* **11**, 5849 (2020).
59. Duan, J. et al. Synthetic access to a framework-stabilized and fully sulfided analogue of an Anderson polyoxometalate that is catalytically competent for reduction reactions. *J. Am. Chem. Soc.* **145**, 7268–7277 (2023).
60. Rabbani, S. M. G. et al. Elucidating the geometric and electronic structure of a fully sulfided analog of an Anderson polyoxomolybdate cluster. *J. Mater. Chem. A* **13**, 32382–32390 (2025).
61. Álvarez-Moreno, M. et al. Managing the computational chemistry big data problem: the ioChem-BD platform. *J. Chem. Inf. Model.* **55**, 95–103 (2015).
62. Bo, C., Maseras, F. & López, N. The role of computational results databases in accelerating the discovery of catalysts. *Nat. Catal.* **1**, 809–810 (2018).
63. H2-reduced_POM_catalyze_hydrogenation_of_CO2_to_methanol. *ioChem-BD* https://doi.org/10.19061/iochem-bd-6-616 (2026).
64. Zhao, Y. & Truhlar, D. G. A new local density functional for main-group thermochemistry, transition metal bonding, thermochemical kinetics, and noncovalent interactions. *J. Chem. Phys.* **125**, 194101 (2006).
65. Weigend, F. Accurate Coulomb-fitting basis sets for H to Rn. *Phys. Chem. Chem. Phys.* **8**, 1057–1065 (2006).
66. Luchini, G., Alegre-Requena, J. V., Funes-Ardoiz, I. & Paton, R. S. GoodVibes: automated thermochemistry for heterogeneous computational chemistry data. *F1000Res.* **9**, 291 (2020).
67. Grimme, S. Supramolecular binding thermodynamics by dispersion-corrected density functional theory. *Chem. Eur. J.* **18**, 9955–9964 (2012).
68. Campbell, C. T. & Sellers, J. R. V. The entropies of adsorbed molecules. *J. Am. Chem. Soc.* **134**, 18109–18115 (2012).
69. Wesselbaum, S. et al. Hydrogenation of carbon dioxide to methanol using a homogeneous ruthenium–Triphos catalyst: from mechanistic investigations to multiphase catalysis. *Chem. Sci.* **6**, 693–704 (2015).
70. Mondal, B., Neese, F. & Ye, S. Toward rational design of 3D transition metal catalysts for CO_2 hydrogenation based on insights into hydricity-controlled rate-determining steps. *Inorg. Chem.* **55**, 5438–5444 (2016).
71. Zhao, Y. & Truhlar, D. G. The M06 suite of density functionals for main group thermochemistry, thermochemical kinetics, noncovalent interactions, excited states, and transition elements: two new functionals and systematic testing of four M06-class functionals and 12 other functionals. *Theor. Chem. Acc.* **120**, 215–241 (2008).
72. Stephens, P. J., Devlin, F. J., Chabalowski, C. F. & Frisch, M. J. Ab initio calculation of vibrational absorption and circular dichroism spectra using density functional force fields. *J. Phys. Chem.* **45**, 11623–11627 (1994).
73. Chai, J. & Gordon, M. H. Long-range corrected hybrid density functionals with damped atom-atom dispersion corrections. *Phys. Chem. Chem. Phys.* **10**, 6615–6620 (2008).

Acknowledgements

This work was initially supported as part of the Inorganometallic Catalyst Design Center, an Energy Frontier Research Center (EFRC) funded by the US Department of Energy (DOE), Office of Science, Basic Energy Sciences (grant no. DE-SC0012702) and subsequently as part of the Catalyst Design for Decarbonization Center EFRC (grant no. DE-SC0023383). This research used the beamline 5-ID-D for X-ray adsorption spectroscopy and 11-ID-B for total scattering measurements at APS, a US DOE Office of Science User Facility operated for the DOE Office of Science by Argonne National Laboratory under contract no. DE-AC02-06CH11357. We thank L. C. Gallington and Q. Ma for help with remote measurements at the beamline and C. J. Tassone (SLAC National Accelerator Laboratory) for sharing beamtime at the APS for the in situ measurements.

Author contributions

Q.L., S.M.G.R. and Z.H. contributed equally to this work. Q.L. conducted the experimental work, analysed the data and prepared the original draft. Z.H. conducted catalysis experiments. S.M.G.R. and R.B.G. performed DFT modelling and calculations. Z.C. and K.W.C. contributed to the PDF and DED experiments. H.Y. helped revise the manuscript. Q.L., W.B., R.B.G. and J.T.H. designed the study and revised the paper. All authors participated in the discussion and data analysis. All authors have given approval for the final version of the manuscript.

Competing interests

J.T.H. has an equity interest in NuMat Technologies, a company that commercializes MOFs. The other authors declare no competing interests.

Additional information

Supplementary information The online version contains supplementary material available at https://doi.org/10.1038/s41557-026-02104-x.

Correspondence and requests for materials should be addressed to Zhihengyu Chen, Wentuan Bi, Rachel B. Getman or Joseph T. Hupp.

Peer review information *Nature Chemistry* thanks Donghai Mei, Weimin Xuan and the other, anonymous, reviewer(s) for their contribution to the peer review of this work.